Ahmad *et al. Adv Struct Chem Imag (2016) 2:9*
DOI 10.1186/s40679-016-0023-0

Advanced Structural and Chemical Imaging

RESEARCH Open Access

Growth of dendritic nanostructures by liquid-cell transmission electron microscopy: a reflection of the electron-irradiation history

Nabeel Ahmad[1], Yann Le Bouar[2], Christian Ricolleau[1] and Damien Alloyeau[1*]

Abstract

Studying dynamical processes by transmission electron microscopy (TEM) requires considering the electron-irradiation history, including the instantaneous dose rate and the cumulative dose delivered to the sample. Here, we have exploited liquid-cell TEM to study the effects of the electron-irradiation history on the radiochemical growth of dendritic Au nanostructures. Besides the well-established direct link between the dose rate and the growth rate of the nanostructures, we demonstrate that the cumulative dose in the irradiated area can also induce important transitions in the growth mode of the nanostructures. By comparing in situ observations with an extended diffusion-limited aggregation model, we reveal how the shape of the nanostructures is severely affected by the local lack of metal precursors and the resulting restricted accessibility of gold atoms to the nanostructures. This study highlights the effects of electron irradiation on the solution chemistry in the irradiated area and in the whole liquid cell that are of primary importance to extract quantitative information on nanoscale processes.

Keywords: Liquid-cell transmission electron microscopy, Electron dose, Diffusion-limited aggregation, Dendritic nanostructures

Background

Liquid-cell transmission electron microscopy (LCTEM) has opened up the opportunity to exploit the analytical and imaging performances of electron microscopes for studying the interfaces between solids and liquids [1]. This technical breakthrough brings new perspectives to the understanding of nanomaterials and soft materials dynamics, electrochemistry, and many geological and biological phenomena [2–5]. Nevertheless, maximising the potential of LCTEM in materials, life and earth sciences require scrutinizing the effects of the electron beam on the dynamical processes under study. When TEM samples are made of liquid, high-energy electrons induce the formation of radiolysis products that drastically change the solution chemistry in the irradiated area. In the case of water, it was demonstrated that the equilibrium concentrations of the primary radiolysis products, including strong reducing and oxidizing species, are reached after a millisecond of irradiation and vary as power laws of the dose rate ($\dot{d}$) [6]. Besides the necessity to consider $\dot{d}$ at any time point, nanoscale processes can also differ over time in the liquid cell, which stresses the impact of the total dose (d_{tot}) in the irradiated area or in the whole volume [7]. Consequently, conclusive LCTEM experiments require understanding the effects of the electron-irradiation history on each sample. In front of the inherent artefacts of LCTEM, two strategies can be employed: minimize them or exploit them. On one hand, radiochemical effects of the electron beam can simply misrepresent the results. This includes, for instance, the very brief viability of live cells under electron irradiation [8] making it challenging to study biochemical processes in real time or the beam-induced growth/etching of nanomaterials [6] that may interfere with electrochemical processes in battery operation

*Correspondence: damien.alloyeau@univ-paris-diderot.fr
[1] Laboratoire Matériaux et Phénomènes Quantiques, UMR7162 Université Paris Diderot-CNRS, Bâtiment Condorcet, 10 Rue Alice Domon et Léonie Duquet, Case Courrier 7021, 75205 Paris Cedex 13, France
Full list of author information is available at the end of the article

[9, 10]. The first challenge is to determine if there exist thresholds of $\dot{d}$ and d_{tot} below which the observed processes remain unaltered (i.e., below the lethal threshold for biological sample or below the electrolyte damage threshold for operando electrochemical investigations). In that regard, the development of extremely low-dose imaging techniques with significant signal-to-noise ratio has been of ongoing interest [11–14]. On the other hand, radiochemical effects can also be exploited as a tuneable driving force if LCTEM studies are conducted in a dose-dependent manner. Indeed, the straightforward control over the concentration of radiolysis products in water was used to study the effects of reaction kinetic on the growth of metal nanoparticles (NPs) driven by the reduction of metallic precursors by hydrated electrons (e_h^-) [15]. This strategy provides very relevant information on the atomic-scale mechanisms that govern nanocrystal shape during wet-chemical synthesis [16]. Furthermore, as the initial pH and salt concentration within the liquid cell directly affect radiochemical processes, these chemical parameters can also be used to tune the growth rate or the stability of metal NPs [17, 18]. Similarly, as exemplified with carbon nanotubes, $\dot{d}$-dependent LCTEM studies of nanomaterial degradation induced by oxidizing radicals produced by radiolysis are very relevant for understanding the oxidative transformations undergone by nanostructures inside biological organisms [19].

Along that line, we exploit here radiochemical growth processes to study how the electron-irradiation history affects the shape of gold nanostructures. By comparing d_{tot}-dependant observations with an extended diffusion-limited aggregation (DLA) model, we explicitly reveal that the molecular and atomic diffusion processes impact the shape of dendritic nanostructures.

Methods

In situ TEM experiments were realized on a JEOL ARM 200F microscope equipped together with a CEOS aberration corrector for the objective lens and a cold FEG electron source [20, 21]. All the experiments were performed with a 200 kV acceleration voltage. The liquid cells commercialized by Protochips Inc. consist of two silicon wafers with dimensions of 2 × 2 mm and 4.5 × 6 mm, called the small and large E-chips, respectively. Each E-chip has one 550 × 50 µm window covered by a 50 nm thick silicon–nitride amorphous film. A 2.5 µL drop of $HAuCl_4$ (1 mM) aqueous solution was deposited on the electron transparent membrane of the small E-chip. The large E-chip was then placed over the small one with their windows in cross configuration, giving a square field of view of 50 µm edge length. Therefore, the drop of solution was squeezed in-between the two E-chips in a volume defined by the thickness of the gold spacers on the small E-chip (150 nm in our case). The entire chamber was then closed by the lid of the holder tip resulting in a vacuum-sealed liquid cell (Additional file 1: Fig. S1).

Liquid-cell transmission electron microscopy experiments were performed in TEM mode without changing condenser aperture and spot size to maintain a constant beam current (i_e). $\dot{d}$ is usually calculated in electrons/Å^{2}s by dividing i_e by the surface irradiated by the beam (S_b). Remarkably, if the illumination system remains constant during TEM experiments (i.e., if one does not touch the brightness knob), increasing the magnification does not affect $\dot{d}$. Indeed, magnifying a TEM image consists in enlarging the image given by objective lens with the projector system, which neither modifies i_e nor S_b. All the TEM experiments were conducted with the same illumination condition corresponding to $\dot{d} = 155$ electrons/Å^{2}s ($S_b = 0.85$ µm^2 and $i_e = 2$ nA). We measured i_e on both the phosphorescent screen and the dynamic-calibrated CCD camera of the microscope prior inserting the sample. Note that in some areas, the burst of nucleation could be initiated by slightly focusing the beam (i.e., increasing $\dot{d}$), but $\dot{d}$ was immediately reduced to 155 electrons/Å^{2}s after the growth starts. This particular high-dose rate was chosen, because it allows optimizing the range of usable magnification. Note that the cold FEG was frequently flashed (every 3 h) to maintain the variability of the beam current below 10 % during the experiments [21].

Liquid thickness is an important parameter of LCTEM experiment. In general, the thickness of the spacers corresponds to the smallest liquid thickness crossed by the electron beam during the TEM experiment. Indeed, due to the outward bowing of the SiN membranes under vacuum, the smallest liquid thickness is found at the corners of the viewing window [22]. Nevertheless, as we did not use the sample holder in flow mode and we used relatively high $\dot{d}$, the formation of hydrogen bubbles affected the distribution of the water inside the liquid cell. As previously described in [23] and illustrated in Additional file 1: Fig. S1, the formation of a large bubble on the middle of the liquid cell tends to minimize the thickness of the liquid film, which consists in two thin layers adsorbed at the surface of the hydrophilic windows. With this liquid-cell configuration, we estimate the liquid thickness to be around 150 nm near to the corners, while it is certainly below 50 nm in the middle of the windows, where HRTEM contrasts can be observed [2]. Note that the continuous growth of gold nanostructures demonstrates that the liquid cell never dried out. Importantly, corner regions of the liquid cell were used for imaging, excepted when atomic-scale information was necessary to understand the growth processes.

The diffusion-limited aggregation (DLA) was first proposed by Witten and Sander [24, 25] and later further

developed and implemented by Meakin [26, 27]. The DLA model is a good representation of processes, where monomers diffuse and get attached by simple contact. It has been used in many physical contexts, such as electrodeposition phenomena [28], neuron growth [29], or bubbles of helium moving into a liquid media [30]. Several extensions of the initial DLA model have been proposed, for example, using a sticking probability [26], a size distribution of diffusing monomers [31], or including restructuring processes after collision [32].

The model considered in this work is an extension of the original model, where monomers diffuse on a two-dimensional square lattice of 256 * 256 sites. We start with a nucleation seed at the centre of the lattice. This seed can either be a single monomer or be an aggregate of monomers. Another monomer is allowed to walk at random by the first nearest neighbour jumps until it arrives at one of the sites adjacent to occupied sites. Then, the random walk is stopped and several attempts of surface-diffusion jumps are performed. In our model, surface diffusion is mimicked by trying N_s times the first or second nearest neighbour jumps along the surface. The local coordination number of the monomer (i.e., the number of occupied nearest neighbour sites) is computed in the initial and final surface positions, and the surface jump is accepted if the final coordination number is higher. In the case of equal coordination numbers, the jump is accepted with a probability equal to 1/2.

In this work, we have tested two different ways of inserting a new diffusing monomer on the lattice. The first choice, which corresponds to the classical DLA algorithm, is to randomly select the position of the new monomer on a circle of radius $R + d_{R,}$ where R is the radius of the aggregate and d_R is a positive radius increment. If d_R is chosen large enough, this represents the process of a diffusing monomer from far away. The second choice is a random insertion of a monomer inside a given circular region of radius R_h. This nucleation process is inspired from the precipitation process occurring under the electron beam studied in this work. Finally, to increase the efficiency of the algorithm, a walking monomer is removed from the simulation if it diffuses too far away from the aggregate, i.e., when the distance to the aggregate is larger than $R + D_{R,}$ where $D_R \gg d_R$. This simple modification saves a significant computational time [33, 34].

Results and discussion

Liquid-cell transmission electron microscopy experiments were conducted in TEM mode with a high and constant $\dot{d}$ of 155 electrons/Å^{2}s on an aqueous solution of $HAuCl_4$ (see "Method" section for details). When a new area of the sample is irradiated by the electron beam, radiologically produced e_h^- reduce gold precursors and the nucleation of gold nanoparticles is quasi-instantaneously observed. Then, nanostructures of several hundred nanometers grow very rapidly along the window plane because of the thin-film geometry of the liquid layer (Fig. 1a, b). The previous reports have demonstrated that the growth rate of metal NPs formed under high $\dot{d}$ is limited by the diffusion of metal precursor to the nanostructures [35, 36]; nevertheless, many diffusion-related effects on the shape of the whole nanostructure remain to be clarified.

In-focus imaging of this fast NP formation was facilitated by polymer-coated gold nanorods deposited on the small E-chip (top membrane in the microscope, Additional file 1: Fig. S1) prior sealing the liquid cell (Fig. 1a, b, t = 0 s). These nanorods also allow differentiating the NPs growing on the top or on the bottom window. Surprisingly, although the electron dose certainly increases at the vicinity of those nanorods, because these latter generate many secondary electrons, gold NPs systematically nucleate and grow on the SiN membrane and seem unaffected by the nanorods. The PEG functionalization could possibly affect the surface chemistry of the nanorods and prevent the adsorption of additional gold atoms.

We quantify the degree to which a nanostructure fills its spatial domain by calculating its filling degree (F_d), corresponding to the ratio between its surface area and the one of its circumscribed circle. In pristine areas, where the total dose is quasi-null at t = 0, we observe the formation of very dense nanostructures with high F_d. The shape of the NPs may differ from a pristine area to another. F_d varies from 65 % for rounded NPs with very large excrescences (Fig. 1a) to 95 % for spherical NPs (Fig. 1b). Nevertheless, this shape-dependant value of F_d is reached a few seconds after nucleation and remains constant during the subsequent growth. Figure 1c shows that apart from the first few seconds of growth, the variation of F_d never exceeds 5 % in pristine areas. Furthermore, this in situ study reveals that NPs observed in the same video may present very different growth dynamics. The time dependence of the NP growth can be approximated with a power law, $R \sim t^{\alpha}$, with R corresponding here to the radius of the nanostructure-circumscribed circle. Consistent with the very large size dispersion of the NPs, α varies greatly from one particle to another. Remarkably, our observations clearly show the influence of the nucleation location on the growth kinetic. Indeed, Fig. 1d, e reveals the boosted growth (α ranges from 0.2 to 0.55) and the broader size dispersion ($\bar{R} = 104 \pm 64$ nm at t = 42 s) of the NPs on the top window as compared to the NPs formed on the bottom window (on which α remains below 0.26 and $\bar{R} = 63 \pm 13$ nm at t = 42 s). This result highlights the disparity in $\dot{d}$ within the liquid cell

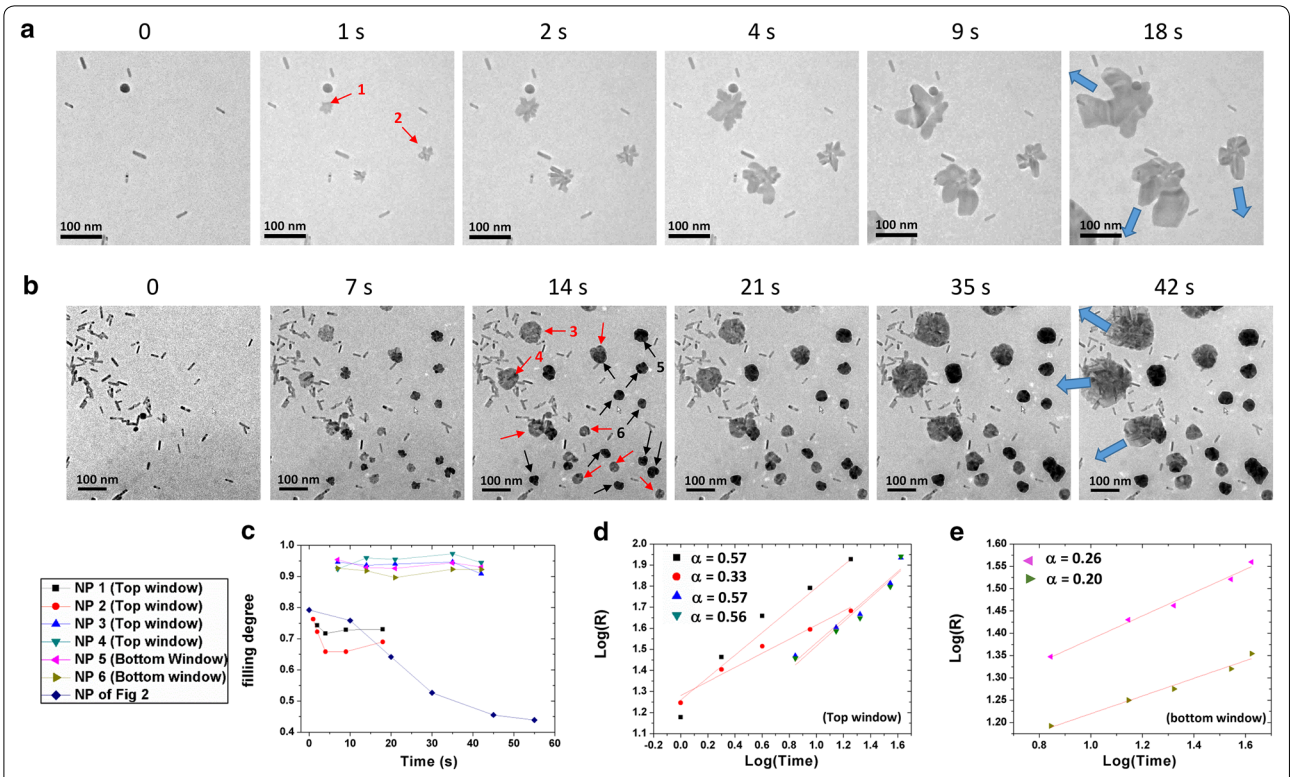

Fig. 1 Growth of gold nanostructures with high F_d in pristine areas (total dose at t = 0 is quasi-null). **a**, **b** LCTEM image series acquired with $\dot{d} = 155$ electrons/Å^{2}s. Gold nanorods deposited on the *top window* during sample preparation are seen on the images at t = 0. *Red arrows* indicate the NPs growing on the *top window* (same focus than the nanorods), whereas *black arrows* show the NPs growing on the *bottom window*. *Blue arrows* highlight the in-plane growth directions of the NPs. Acquisition time is indicated over each image. These two image series were acquired in different areas. **c** Filling degree of NPs as a function of time. **d**, **e** Logarithmic relationship between the radius of nanostructure-circumscribed circle and time for NPs on the *top* and *bottom windows*, respectively. The *red curves* show that the linear fits of the data points and the slopes of these fits (α) are indicated. All the data in Fig. 1c–e are measured on the NPs labelled from 1 to 6 in Fig. 1a, b and the NP in Fig. 2

which is known to decrease with the depth in the liquid film due to electron absorption [37]. This disparity in the NP growth rate makes it difficult to compare these experimental data with the Lifshitz–Slyozov–Wagner growth model [38]. Although the growth speed is affected by the $\dot{d}$-dependant concentration of reducing agent, F_d remains similarly constant and high on both membranes (Fig. 1c).

Interestingly, the growth mechanisms in areas, where the total dose is non-null before observation, lead to the formation of dendritic nanostructures with much lower F_d. Figure 2 shows the growth of sharp dendrites over a nearly spherical nanoparticle formed during the 45 s of pre-exposure (d_{tot} before dendritic growth is 6975 electrons/A^2). This result highlights a transition in the growth mechanisms of the NPs. In view of the time dependency of R (Fig. 1d, e), after 45 s of pre-exposure, the growth of spherical nanoparticles is very slow. The burst of nucleation of the dendrites was initiated by slightly focusing the beam (i.e., increasing $\dot{d}$), but $\dot{d}$ was immediately reduced to 155 electrons/Å^{2}s after the growth starts. Then, the growth of tree-like structures homogeneously distributed over the surface of the spherical NP induces a drastic drop of F_d, from 79 to 43 % in 55 s (Fig. 1e).

We have exploited an extended DLA model to describe in a didactic way the mechanisms affecting the shape of gold nanostructures during growth. In these simulations of aggregate growth, the flux of matter is ensured by inserting random walkers (i.e., monomers) on a 2D square lattice with a single nucleation seed at the centre of the square. As soon as a monomer visits a site adjacent to this nucleation seed, it becomes part of the growing aggregate (see "Method" section for details). Although this model does not account for the energy landscape of the nanoparticles, it allows considering the effect of monomer-diffusion pathway on the shape of the aggregate. Figure 3a shows the general appearance of the 2D structures obtained when the monomers are randomly inserted inside a circular area around the nucleation seed. These conditions simulate the growth of an NP by adsorption of single atoms with a homogeneous local concentration of precursors. The circular area around the nucleation seed corresponds then to the electron beam

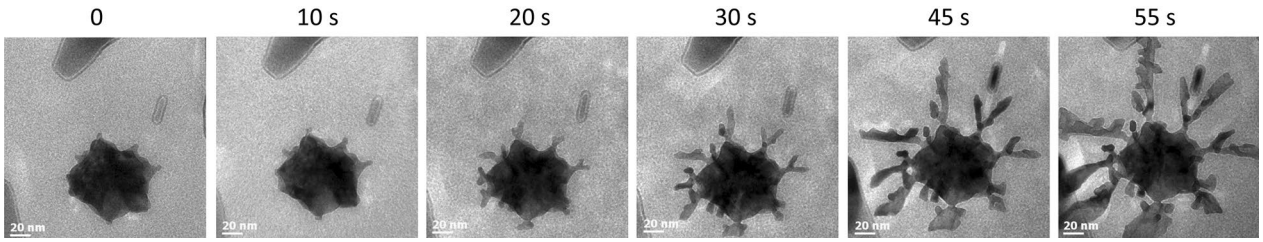

Fig. 2 Growth of dendritic nanostructures in pre-exposed area. LCTEM image series acquired with $\dot{d} = 155$ electrons/Å^{2}s. After irradiating a large area for 45 s (total dose at t = 0 s is 6975 electron/Å^2), TEM imaging was magnified to follow the growth of sharp dendrites on nearly spherical NPs. The filling degree of the whole NP is reduced from 79 % at t = 0 s to 43 % at t = 55 s (see Fig. 1e). Acquisition time is indicated over each image

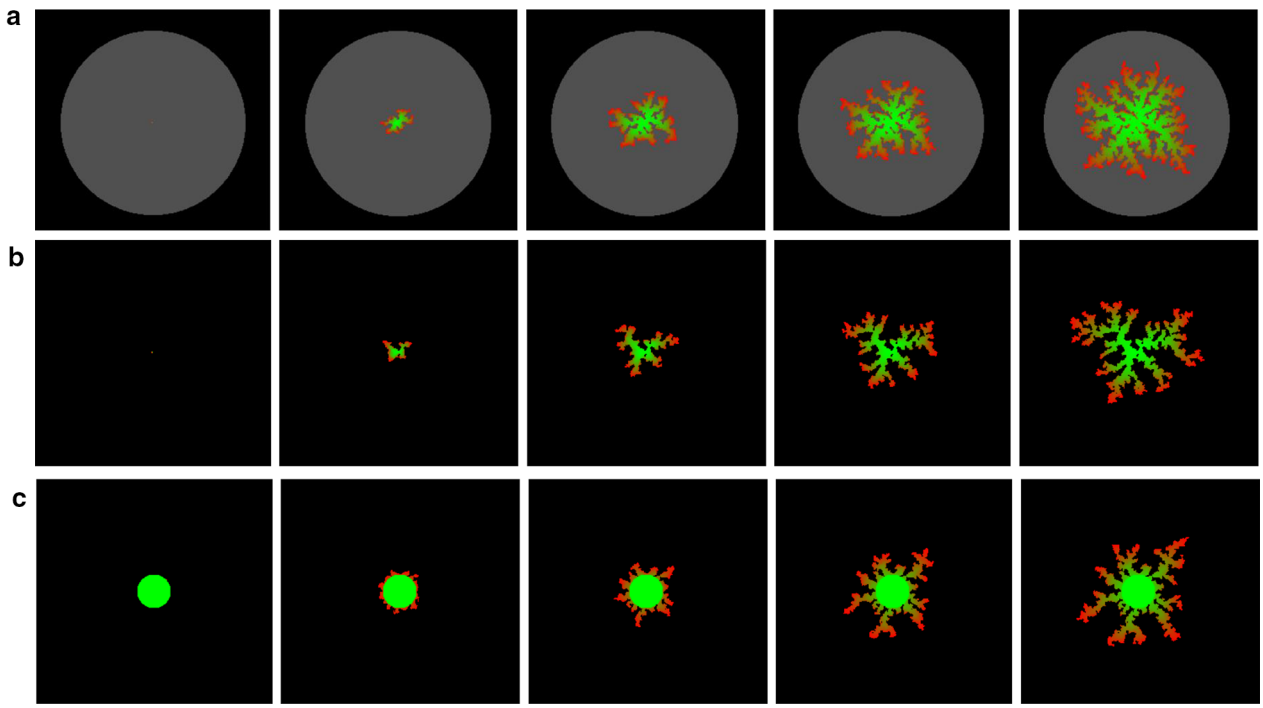

Fig. 3 Aggregate growth calculated with the extended DLA model. The square lattice is made of 256 * 256 sites, and the number of surface-diffusion steps is 20. **a** Diffusing monomers randomly appear inside the *bright area* with a radius of 110 lattice spacings. **b** Monomers are inserted far away from the growing structure. This latter is a single site at the beginning of the simulation **c** Monomers are inserted far away from the growing structure. This latter is a circular particle of 20 lattice-spacing radius at the beginning of the simulation. The *green-to-red* color scale indicates the time at which aggregation occurred: the oldest aggregation events appear in *green* and the most recent in *red*

irradiating a pristine area during LCTEM experiments. Growth in homogenous concentration always generates dense structures, with F_d of almost 50 % when R of the aggregates reaches 100 lattice spacings (Fig. 4). Note that larger F_d are obtained at longer time (i.e., larger R), since monomers keep appearing in empty sites of the lattice. The growth model was used to display the effect of a depletion of monomer at the vicinity of a nucleation seed. Indeed, when random walkers are inserted far away from the nucleation seed (classical DLA conditions, see "Method" section), the extended diffusion pathway of the monomers induces the growth of dendritic structures (Fig. 3b), with F_d below 25 % when R of the aggregates reach 100 lattice spacings (Fig. 4). Figure 3c shows that similar dendritic growth is observed when the central nucleation seed is a circular aggregate. As observed by LCTEM, the dendrites are then homogenously distributed over the surface of circular seed and F_d drops from 100 to 25 %, while R increases from 20 to 100 lattice spacings (Fig. 4).

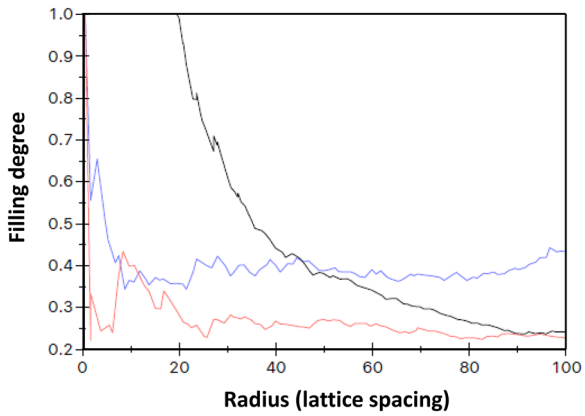

Fig. 4 Filling degree as a function of the radius of the structures measured on the DLA simulations. *Blue curve*: NP of Fig. 3a. *Red curve*: NP of Fig. 3b. *Black curve*: NP of Fig. 3c

These simulations allow recapitulating the effects of the history of dose delivery on the growth processes of gold nanostructures. When following the growth in pristine areas, the abundance of Au precursors under the beam induces the growth of dense nanostructures with high F_d. The growth velocity then depends on both the local $\dot{d}$ (which depends on the observed window) and the concentration of precursors. When following the growth in a pre-exposed area, the formation of nanostructures during the pre-exposure time creates a depletion of precursors in the irradiated area. The subsequent growth is then kinetically limited by the diffusion of precursors from unexposed regions to the electron beam and the diffusion of the monomer to the nanostructures. This inward flow of matter favours the formation of dendrites and reduces F_d, because the probability for gold atoms to reach the central NP drastically decreases with the spreading of the tree-like structure.

If the dendritic structures of NPs in pre-exposed area are the signature of DLA growth, one may wonder whether monomer/precursor diffusion also affects the shape of the NPs in pristine areas. This relevant question can first be tackled by estimating the consumption rate of gold precursors within the volume of interaction. Considering the precursor concentration of 1 mM, the beam surface of 0.85 μm^2 and a constant liquid thickness of 150 nm, we can estimate that the irradiated volume contains 7.7 10^4 $HAuCl_4$ molecules before irradiation. During LCTEM observations, this volume is irradiated with a dose rate of 1.3 10^{10} electrons/s. By studying the growth of gold nanoplates of known thickness with similar illumination conditions and $\dot{d}$, Park and co-workers have estimated that the reduction of one Au^{3+} ion to Au atom requires 6000 primary electrons with an energy of 300 kV [17]. As reducing the kinetic energy of primary electrons from 300 to 200 kV increases the energy density-normalized stopping power of water by 18 %, we can estimate that in our LCTEM study, 4920 primary electrons are necessary to reduce one Au^{3+} ions. Therefore, the electron beam can potentially consume 2.6 10^6 $HAuCl_4$ molecules per second. All these estimations directly depend on the local thickness of liquid that is roughly estimated here. Nevertheless, we can conclude that the consumption of all the gold precursors in the irradiated volume before irradiation takes in fact much less than a second. In addition, 7.7 10^4 precursors could only generate a total volume of Au nanocrystals of 2.6 10^3 nm^3 (equivalent to a 14 nm nanocube) which is obviously much less than the total volume of gold NPs formed experimentally. Therefore, precursors coming from external areas of the beam are necessary to supply the growth of nanostructures of several hundred nanometers observed in pristine areas. This flow of matter is ensured by the diffusion of $HAuCl_4$ molecules. The diffusion coefficient of molecular species in water is known to vary linearly with their formula weight and the temperature. This linear relationship reviewed by Hobbie et al. [39] allows estimating the diffusion coefficient of $HAuCl_4$ in aqueous solution at 20 °C to be around 0.5 10^{-9} m^2/s, meaning that in 1 s, a molecule $HAuCl_4$ can spread over 500 μm^2. This very efficient homogenisation of the solution concentration is in competition with the local beam-induced consumption of gold precursors and delays the creation of a concentration depletion around the NPs. This explains the fast formation of dense nanostructures in pristine areas. Nevertheless, after approximatively 15 s of observation, the first effects of the lack of precursors around the NPs can be identified. Figure 1a, b shows that the isotropic NPs at the early stage of the growth transform into anisotropic nanoparticles with anisotropy axes pointing to different directions (indicated by blue arrows). This growth anisotropy of the nanostructures is even more pronounced at longer time (Additional file 1: Fig. S2). As exemplified in the simulation shown in Fig. 5, this transition in the growth mechanisms arises from an inter-particle screening effect that is characteristic of DLA growth [36, 40]. We ran DLA simulations with three nucleation seeds on the square lattice. In homogenous concentration condition, the three aggregates grow isotopically and finally coalesce (Fig. 5b). On the contrary, when the monomers are inserted far away from the nucleation seeds, the three aggregates grow along opposite outward directions (Fig. 5a), because the probability for a monomer to reach the region in-between the three NPs decreases, as the size of anisotropic nanostructure increases. This screening effect has a tremendous impact on the shape of the nanostructures, because it governs the directionality of

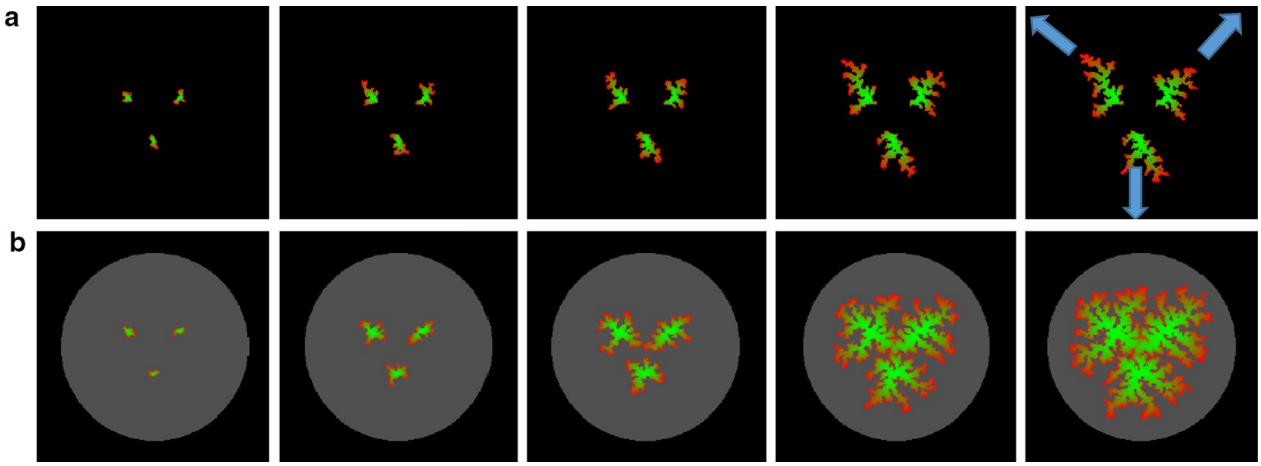

Fig. 5 Growth of three aggregates calculated with the extended DLA model. The square lattice is made of 256 * 256 sites and contains three nucleation seeds (single sites at the beginning of the simulation). The number of surface-diffusion steps is 20. **a** Monomers are inserted far away from the growing structures. *Blue arrows* highlight the growth directions of the NPs. **b** Monomers randomly appear inside the *bright area* with a radius of 110 lattice spacings. There is no preferential growth direction. The *green-to-red* color scale indicates the time at which aggregation occurred: the oldest aggregation events appear in *green* and the most recent in *red*

the growth, it prevents coalescence events and it also drives the tree-like structure of dendritic nanostructures.

It is worth noticing that given the potential consumption rate of gold precursors and the density of molecule per μm^3, 15 s necessary to start observing the screening effects correspond to the time necessary for the beam to potentially consume all the precursors over an area of 428 μm^2. This large lack of precursors cannot be counter-balanced by molecular diffusion anymore, and the growth directions of the NPs are then dictated by external-concentration gradients. Such characteristic transitions in the growth processes of nanomaterials could serve to evaluate the very dynamic and heterogeneous nature of local molecular concentrations during LCTEM observations. This also allows realizing that when the flow capabilities of the in situ sample holder are not used, precursor supply in the liquid cell irradiated with high $\dot{d}$ is far from inexhaustible. The fast depletion of the mean concentration of metal precursors within the whole liquid cell explains the slowdown of the NPs growth rate measured over time when many pristine areas are consecutively analysed [7].

Finally, atomic-scale monitoring of nanostructure growth reveals that crystal reshaping can also affect the final morphology of the nanostructures. The tendency of nanocrystals to form energetically stable shapes is always in competition with the flux of atoms adsorbing on their surface. When the growth is fast (Fig. 1a, b), crystal shape is dominated by kinetic effects leading to the disappearance of highly concave surface structure, because the chemical potential of surfaces is inversely proportional to their curvature. This surface-diffusion mechanism tends to smooth NP surface and to form rounded and large excrescences. This effect can be simulated in our growth model by tuning the ability of adsorbed monomer to diffuse over the aggregate surface to reach sites of higher coordination. Figure 6 shows that increasing surface diffusion leads to the formation of larger dendrites and increases F_d of the nanostructure. When NP growth is slowed down by the weak availability of precursors in the local environment, the growth is then significantly impacted by thermodynamic effects and faceting of the dendrites is observed (Fig. 7). HRTEM imaging reveals that low-index crystal facets, such as (111) and (020), are preferentially formed, together with (111) planar defects most likely to relax the elastic strength accumulated during crystal growth and reshaping.

Conclusions

By comparing d_{tot}-dependant LCTEM observations with an extended DLA growth model, we have demonstrated that the cumulative aspect of the electron dose can severely impact the growth mechanisms of gold nanostructures, because it affects both the availability of metal precursors and the accessibility of gold atoms to the NPs. High $\dot{d}$ irradiation of a pristine area of the liquid cell generates the growth of high F_d nanostructures and consequently creates a depletion of gold precursors in and around the irradiated area. In subsequent observations, this heterogeneous distribution of the precursors drives transformations in the nanostructure shape from isotropic to anisotropic or

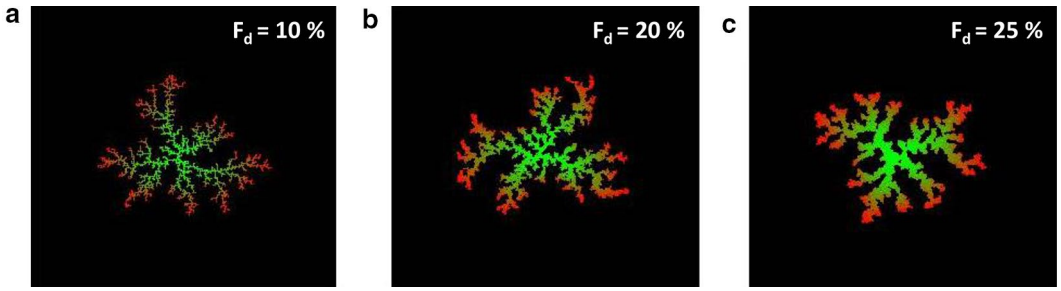

Fig. 6 Effect of surface diffusion on the shape of aggregates obtained with the DLA growth model. The square lattice is made of 256 * 256 sites. The monomers are inserted far away from the growing structure that is a single site at the beginning of the simulation. The number of surface-diffusion step is 1 (**a**), 10 (**b**), and 20 (**c**). The filling degree of the aggregates is indicated on each image. The *green-to-red color* scale indicates the time at which aggregation occurred: the oldest aggregation events appear in *green* and the most recent in *red*

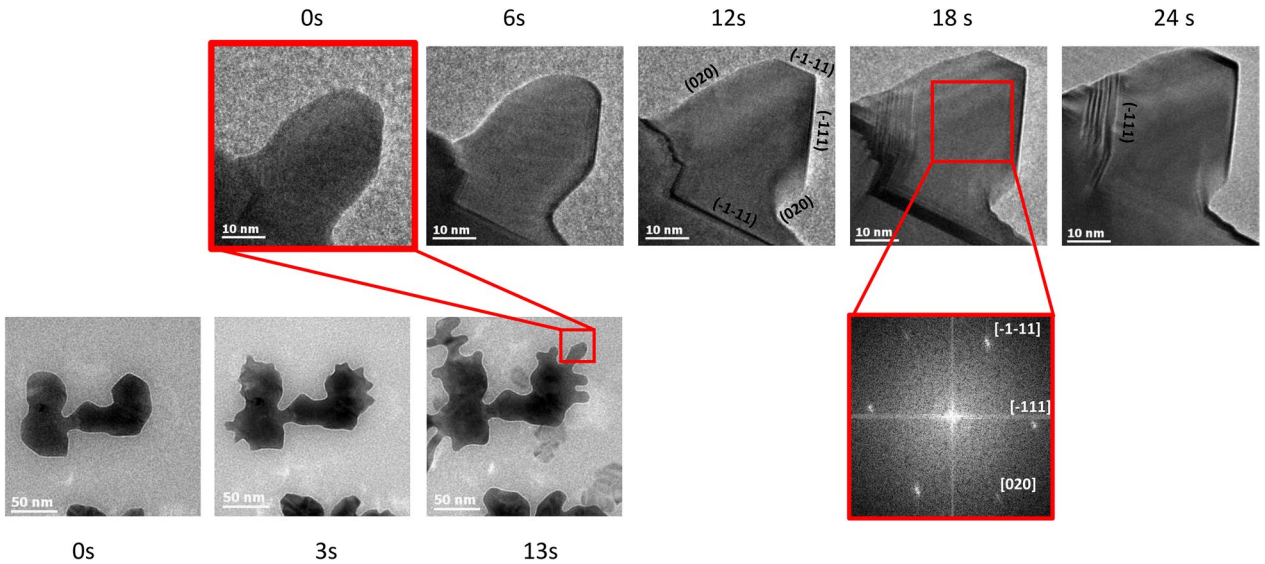

Fig. 7 Reshaping of dendrites by surface diffusion and crystal faceting. *Bottom images*: growth of sharp dendrites on a large aggregate of NP. *Top images*: TEM imaging was then magnified to follow the reshaping of a dendrite at high resolution (time scale is reset to zero). Surface-diffusion mechanisms tend to form (111)- and (002)-type facets. These phenomena tend to enlarge the dendrite. Facet indexes are deduced from the FFT of the image acquired at t = 18 s (*bottom right*) showing the FCC structure of gold oriented along the [101] zone axis

dendritic morphologies. This transition in the growth mode is imposed by the extended diffusion time of precursors to the irradiated area and a resulting screening effect that imposes directional growth and tree-like structures with low F_d. As thermodynamic and kinetic effects are always in competition during NP formation, nanocrystal faceting can also reshape the dendrites when the growth is slow. More generally, these results illustrate that the history of the electron dose, combining the instantaneous $\dot{d}$ and the cumulative dose delivered to the sample, is a key parameter that cannot be ignored when analysing or designing in situ experiments. Finally, the python program used here to models DLA growth is available in supplementary materials. DLA processes, in which atoms, NPs, or other nano-objects randomly diffuse and cluster together to form dendritic aggregates, are frequently observed in LCTEM experiments. Therefore, we hope this code and its further developments will help interpreting other growth phenomena.

Additional file

Additional file 1: Figure S1. Schematic cross section of the sealed liquid cell in the JEOL ARM microscope under high-dose rate.

Figure S2. Anisotropic nanostructures formed after 2 min observation in pristine area. Two python programs that model DLA growth, in classical DLA conditions (namely, DLA_sticking.py) and in homogenous concentration conditions (namely, DLA_sticking_homogen_nucl.py).

Authors' contributions

DA, NA, and CR conducted the liquid-cell TEM experiments. DA and NA analysed the experimental data. YLB developed and ran the DLA simulations. DA wrote the manuscript. All authors read and approved the final manuscript.

Author details

[1] Laboratoire Matériaux et Phénomènes Quantiques, UMR7162 Université Paris Diderot-CNRS, Bâtiment Condorcet, 10 Rue Alice Domon et Léonie Duquet, Case Courrier 7021, 75205 Paris Cedex 13, France. [2] Laboratoire d'Etude des Microstructures, ONERA/CNRS, B.P. 72, 92322 Châtillon, France.

Acknowledgements

The authors gratefully acknowledge stimulating discussions with Dr. A. Finel on the diffusion-limited aggregation. We also acknowledge the financial support of the Region Ile-de-France (convention SESAME E1845 for the JEOL ARM 200F electron microscope installed at the Paris Diderot University), the Labex SEAM (Plas-Mag project), and the CNRS (Defi-Nano Program).

Competing interests

The authors declare that they have no competing interests.

Received: 3 March 2016 Accepted: 21 June 2016
Published online: 30 June 2016

References

1. Williamson, M.J., Tromp, R.M., Vereecken, P.M., Hull, R., Ross, F.M.: Dynamic microscopy of nanoscale cluster growth at the solid-liquid interface. Nat. Mater. **2**(8), 532–536 (2003)
2. de Jonge, N., Ross, F.M.: Electron microscopy of specimens in liquid. Nat. Nanotechnol. **6**(11), 695–704 (2011)
3. Liao, H.G., Niu, K.Y., Zheng, H.M.: Observation of growth of metal nanoparticles. Chem. Commun. **49**(100), 11720–11727 (2013)
4. Ngo, T., Yang, H.: Toward ending the guessing game: study of the formation of nanostructures using in situ liquid transmission electron microscopy. J. Phys. Chem. Lett. **6**(24), 5051–5061 (2015)
5. Ross, F.M.: Opportunities and challenges in liquid cell electron microscopy. Science. **350**(6267), 1490 (2015)
6. Schneider, N.M., Norton, M.M., Mendel, B.J., Grogan, J.M., Ross, F.M., Bau, H.H.: Electronâ€ water interactions and implications for liquid cell electron microscopy. J. Phys. Chem. C **118**(38), 22373–22382 (2014)
7. Abellan, P., Woehl, T.J., Parent, L.R., Browning, N.D., Evans, J.E., Arslan, I.: Factors influencing quantitative liquid (scanning) transmission electron microscopy. Chem. Commun. **50**(38), 4873–4880 (2014)
8. Peckys, D.B., de Jonge, N.: Liquid scanning transmission electron microscopy: imaging protein complexes in their native environment in whole eukaryotic cells. Microsc. Microanal. **20**(02), 346–365 (2014)
9. Holtz, M.E., Yu, Y.C., Gunceler, D., Gao, J., Sundararaman, R., Schwarz, K.A., Arias, T.A., Abruna, H.D., Muller, D.A.: Nanoscale imaging of lithium ion distribution during in situ operation of battery electrode and electrolyte. Nano. Lett. **14**(3), 1453–1459 (2014)
10. Mehdi, B.L., Qian, J., Nasybulin, E., Park, C., Welch, D.A., Faller, R., Mehta, H., Henderson, W.A., Xu, W., Wang, C.M., Evans, J.E., Liu, J., Zhang, J.G., Mueller, K.T., Browning, N.D.: observation and quantification of nanoscale processes in lithium batteries by operando electrochemical (S)Tem. Nano. Lett. **15**(3), 2168–2173 (2015)
11. Carlson, D. B., Evans, J. E.: Low-dose imaging techniques for transmission electron microscopy. In: Maaz, K. (ed) The Transmission Electron Microscope, p. 85. InTech, Rijeka (2012)
12. McMullan, G., Faruqi, A.R., Clare, D., Henderson, R.: Comparison of optimal performance at 300 kev of three direct electron detectors for use in low dose electron microscopy. Ultramicroscopy. **147**, 156–163 (2014)
13. Buban, J.P., Ramasse, Q., Gipson, B., Browning, N.D., Stahlberg, H.: High-resolution low-dose scanning transmission electron microscopy. J. Electron. Microsc. **59**(2), 103–112 (2010)
14. Stevens, A., Yang, H., Carin, L., Arslan, I., Browning, N.D.: The potential for bayesian compressive sensing to significantly reduce electron dose in high-resolution stem images. Microscopy. **63**(1), 41–51 (2014)
15. Woehl, T.J., Evans, J.E., Arslan, I., Ristenpart, W.D., Browning, N.D.: Direct in situ determination of the mechanisms controlling nanoparticle nucleation and growth. ACS. Nano. **6**(10), 8599–8610 (2012)
16. Alloyeau, D., Dachraoui, W., Javed, Y., Belkahla, H., Wang, G., Lecoq, H., Ammar, S., Ersen, O., Wisnet, A., Gazeau, F., Ricolleau, C.: Unravelling kinetic and thermodynamic effects on the growth of gold nanoplates by liquid transmission electron microscopy. Nano. Lett. **15**(4), 2574–2581 (2015)
17. Park, J.H., Schneider, N.M., Grogan, J.M., Reuter, M.C., Bau, H.H., Kodambaka, S., Ross, F.M.: Control of electron beam-induced au nanocrystal growth kinetics through solution chemistry. Nano. Lett. **15**(8), 5314–5320 (2015)
18. Hermannsdorfer, J., de Jonge, N., Verch, A.: Electron beam induced chemistry of gold nanoparticles in saline solution. Chem. Commun. **51**(91), 16393–16396 (2015)
19. Elgrabli, D., Dachraoui, W., Menard-Moyon, C., Liu, X.J., Begin, D., Begin-Colin, S., Bianco, A., Gazeau, F., Alloyeau, D.: Carbon nanotube degradation in macrophages: live nanoscale monitoring and understanding of biological pathway. ACS. Nano. **9**(10), 10113–10124 (2015)
20. Alloyeau, D., Oikawa, T., Nelayah, J., Wang, G., Ricolleau, C.: Following ostwald ripening in nanoalloys by high-resolution imaging with single-atom chemical sensitivity. Appl. Phys. Lett. **101**, 121920 (2012)
21. Ricolleau, C., Nelayah, J., Oikawa, T., Kohno, Y., Braidy, N., Wang, G., Hue, F., Florea, I., Bohnes, V.P., Alloyeau, D.: Performances of an 80–200 Kv microscope employing a cold-feg and an aberration-corrected objective lens. Microscopy. **62**, 283 (2012)
22. Holtz, M.E., Yu, Y., Abruña, H.D., Muller, D.A.: In-situ electron energy loss spectroscopy of liquids. Microsc. Microanal. **18**(SupplementS2), 1094–1095 (2012)
23. Grogan, J.M., Schneider, N.M., Ross, F.M., Bau, H.H.: Bubble and pattern formation in liquid induced by an electron beam. Nano. Lett. **14**(1), 359–364 (2014)
24. Witten, T.A., Sander, L.M.: Diffusion-limited aggregation, a kinetic critical phenomenon. Phys. Rev. Lett. **47**(19), 1400–1403 (1981)
25. Witten, T.A., Sander, L.M.: Diffusion-Limited Aggregation. Phys. Rev. B **27**(9), 5686–5697 (1983)
26. Meakin, P.: Diffusion-controlled cluster formation in 2-dimensional space. Phys. Rev. A **27**(3), 1495–1507 (1983)
27. Meakin, P.: Progress in DLA research. Physica. D. **86**(1–2), 104–112 (1995)
28. Argoul, F., Arneodo, A., Grasseau, G., Swinney, H.L.: Self-similarity of diffusion-limited aggregates and electrodeposition clusters. Phys. Rev. Lett. **61**(22), 2558–2561 (1988)
29. Caserta, F., Stanley, H.E., Eldred, W.D., Daccord, G., Hausman, R.E., Nittmann, J.: Physical mechanisms underlying neurite outgrowth: a quantitative analysis of neuronal shape. Phys. Rev. Lett. **64**(1), 95–98 (1990)
30. Haard, T.M., Gervais, G., Nomura, R., Halperin, W.P.: The pathlength distribution of simulated aerogels. Physica. B. **284–288**(Part 1), 289–290 (2000)

31. Braga, F.L., Mattos, O.A., Amorin, V.S., Souza, A.B.: Diffusion limited aggregation of particles with different sizes: fractal dimension change by anisotropic growth. Physica. A. **429**, 28–34 (2015)
32. Jullien, R., Meakin, P.: Simple models for the restructuring of three-dimensional ballistic aggregates. J. Colloid. Interface. Sci. **127**(1), 265–272 (1989)
33. Lee, S.-L., Luo, Y.-L.: Simulation of diffusion-limited aggregation: effects of launching boundary shape and non-fixed centre. Chem. Phys. Lett. **195**(4), 405–411 (1992)
34. Braga, F.L., Ribeiro, M.S.: Diffusion limited aggregation: algorithm optimization revisited. Comput. Phys. Commun. **182**(8), 1602–1605 (2011)
35. Kraus, T., de Jonge, N.: Dendritic gold nanowire growth observed in liquid with transmission electron microscopy. Langmuir. **29**(26), 8427–8432 (2013)
36. Zhu, G., Jiang, Y., Lin, F., Zhang, H., Jin, C., Yuan, J., Yang, D., Zhang, Z.: In situ study of the growth of two-dimensional palladium dendritic nanostructures using liquid-cell electron microscopy. Chem. Commun. **50**(67), 9447–9450 (2014)
37. Liu, Y., Lin, X.-M., Sun, Y., Rajh, T.: In situ visualization of self-assembly of charged gold nanoparticles. J. Am. Chem. Soc. **135**(10), 3764–3767 (2013)
38. Lifshitz, I.M., Slyozov, V.V.: The kinetics of precipitation from supersaturated solid solutions. J. Phys. Chem. Solids **19**, 35–50 (1961)
39. Hobbie, R. K., Roth, B. J.: Transport in an infinite medium. In: Russell K. H., Roth, B. J. (eds.) Intermediate Physics for Medicine and Biology, pp. 81–109. Springer, Berlin (2007)
40. Vicsek, T.: Fractal growth phenomena. World Scientific, Singapour (1992)